

# Robust Sliding-mode Control of Wind Energy Conversion Systems for Optimal Power Extraction via Nonlinear Perturbation Observers

Bo Yang\*, Tao Yu†, Hongchun Shu\*, Jun Dong\*, Lin Jiang‡

## Abstract

This paper designs a novel robust sliding-mode control using nonlinear perturbation observers for wind energy conversion systems (WECS), in which a doubly-fed induction generator (DFIG) is employed to achieve an optimal power extraction with an improved fault ride-through (FRT) capability. The strong nonlinearities originated from the aerodynamics of the wind turbine, together with the generator parameter uncertainties and wind speed randomness, are aggregated into a perturbation that is estimated online by a sliding-mode state and perturbation observer (SMSPO). Then, the perturbation estimate is fully compensated by a robust sliding-mode controller so as to provide a considerable robustness against various modelling uncertainties and to achieve a consistent control performance under stochastic wind speed variations. Moreover, the proposed approach has an integrated structure thus only the measurement of rotor speed and reactive power is required, while the classical auxiliary dq-axis current regulation loops can be completely eliminated. Four case studies are carried out which verify that a more optimal wind power extraction and an enhanced FRT capability can be realized in comparison with that of conventional vector control (VC), feedback linearization control (FLC), and sliding-mode control (SMC).

**Keyword** DFIG, optimal power extraction, FRT, nonlinear perturbation observer, robust sliding-mode control

---

\*Bo Yang, Hongchun Shu, and Jun Dong are with the Faculty of Electric Power Engineering, Kunming University of Science and Technology, 650500, Kunming, China.

†Tao Yu is with the School of Electric Power Engineering, South China University of Technology, Guangzhou, China. (corresponding author, Email: taoyu1@scut.edu.cn)

‡Lin Jiang is with the Department of Electrical Engineering & Electronics, University of Liverpool, Liverpool, L69 3GJ, United Kingdom.

# 1 Introduction

Due to the astonishingly ever-increasing population issue and environmental crisis, both the social and industrial demands of renewable energy keep growing rapidly in the past decade around the globe. As one of the most abundant and mature renewable energy, wind energy conversion systems (WECS) have been paid considerable attention and their proportion in nationwide energy production will rise even faster in future [1]. Nowadays, the most commonly used wind turbine in WECS is based on doubly-fed induction generator (DFIG) because of its noticeable merits: variable speed generation, the reduction of mechanical stresses and acoustic noise, as well as the improvement of the power quality [2].

So far, an enormous variety of studies have been undertaken for DFIG modelling and control, in which vector control (VC) incorporated with proportional-integral (PI) loops is the most popular and widely recognized framework in industry, thanks to its promising features of decoupling control of active/reactive power, simple structure, as well as high reliability [3]. The primary goal of DFIG control system design is to optimally extract the wind power under random wind speed variation, which is usually called maximum power point tracking (MPPT) [4]. Meanwhile, a fault-ride through (FRT) capability is often required so that DFIG can withstand some typical disturbances in power grids [5]. However, one significant drawback of VC is that it cannot maintain a consistent control performance when operation conditions vary as its PI parameters are determined by the one-point linearization, while DFIG is a highly nonlinear system resulted from the fact that it frequently operates under a time-varying and wide operation region by stochastic turbulent wind. Several optimal parameter tuning techniques have been examined to improve the overall control performance of PI control, such as the differential evolutionary algorithm (DE) employed for the performance enhancement of DFIG in the presence of external disturbances [6]. Reference [7] proposed a meta-heuristic algorithm called grouped grey wolf optimizer to achieve MPPT together with an improved FRT capability. In addition, literature [8] adopted particle swarm optimizer (PSO) to enhance the building energy performance. Moreover, a genetic algorithm was developed to minimize the energy consumption of the hybrid energy storage system in electric vehicle [9].

On the other hand, plenty of promising alternatives have been investigated attempting to remedy such inherent flaws of VC. For example, fuzzy-logic was used to deal with onshore wind farm site selection [10]. In reference [11], a feedback linearization control (FLC) was designed for MPPT of DFIG with a thorough modal analysis of generator dynamics, which internal dynamics stability is also proved in the context of Lyapunov criterion. Besides, both the rotor position and speed are calculated based on model reference adaptive system (MRAS) control strategy by [12], such that a fast dynamic response without the requirement of flux estimation can be realized. Furthermore, a robust continuous-time

33 model predictive direct power control of DFIG was proposed via Taylor series expansion for stator current  
34 prediction, which is directly used to compute the required rotor voltage in order to minimize the difference  
35 between the actual stator currents and their references over the prediction period [13]. Meanwhile,  
36 literature [14] developed an internal model state-feedback approach to control the DFIG currents, which is  
37 able to provide robustness to external disturbances automatically and to eliminate the need of disturbance  
38 compensation. Additionally, a Lyapunov control theory based controller was devised for rotor speed  
39 adjustment without any information about wind data or an available anemometer [15]. A nonlinear  
40 robust power controller based on a hybrid of adaptive pole placement and backstepping was presented  
41 in [16], which implementation feasibility is validated through field-programmable gate array (FPGA).  
42 Moreover, an approximate dynamic programming based optimal and adaptive reactive power control  
43 scheme was applied to remarkably improve the transient stability of power systems with wind farms [17].

44 Among all sorts of advanced approaches, sliding-mode control (SMC) is a powerful high-frequency  
45 switching control scheme for nonlinear systems with various uncertainties and disturbances, which elegant-  
46 ly features effective disturbance rejection, fast response, and strong robustness [18], thus it is appropriate  
47 to tackle the above obstacles. In work [19], the dynamics of a small-capacity wind turbine system con-  
48 nected to the power grid was altered under severe faults of power grids, in which the transient behaviour  
49 and the performance limit for FRT are discussed by using two protection circuits of an AC-crowbar and  
50 a DC-Chopper. A high-order SMC was applied which owns prominent advantages of great robustness  
51 against power grid faults, together with no extra mechanical stress on the wind turbine drive train [20].  
52 In addition, reference [21] wisely chose a sliding surface that allows the wind turbine to operate very  
53 closely to the optimal regions, while PSO was used to determine the optimal slope of the sliding surface  
54 and the switching component amplitude. Further, an intelligent proportional-integral SMC was proposed  
55 for direct power control of variable-speed constant-frequency wind turbine systems and MPPT under  
56 several disturbances [22]. Moreover, literature [23] designed a robust fractional-order SMC for MPPT  
57 and robustness enhancement of DFIG, in which unknown nonlinear disturbances and parameter uncer-  
58 tainties are estimated via a fractional-order uncertainty estimator while a continuous control strategy is  
59 developed to realize a chattering-free manner.

60 Nevertheless, an essential shortcoming of SMC is its over-conservativeness stemmed from the use of  
61 upper bound of uncertainties, while these worst conditions in which the perturbation takes its upper  
62 bound does not usually occur. As a consequence, numerous disturbance/perturbation observer based  
63 controllers have been examined which aim to provide a more appropriate control performance by real-time  
64 compensation of the combinatorial effect of various uncertainties and disturbances, e.g., a high-gain state

65 and perturbation observer (HGSPPO) was adopted to estimate the unmodelled dynamics and parameter  
 66 uncertainties of multi-machine power systems equipped with flexible alternating current transmission  
 67 system devices, such that a coordinated adaptive passive control can be realized [24]. Alternatively, a  
 68 nonlinear observer based adaptive disturbance rejection control (ADRC) was proposed to improve the  
 69 power tracking of DFIG under abrupt changes in wind speed, which can be applied for any type of  
 70 optimal active power tracking algorithms [25]. Moreover, reference [26] described a linear ADRC based  
 71 load frequency control (LFC) to maintain generation-load balance and to realize disturbance rejection  
 72 of power systems integrated with DFIG. In work [27], sliding-mode based perturbation observer was  
 73 used to design a nonlinear adaptive controller for power system stability enhancement. On the other  
 74 hand, disturbance observer based SMC was studied for continuous-time linear systems with mismatched  
 75 disturbances or uncertainties [28], while the applications of disturbance/perturbation observer based SMC  
 76 can be referred to the current regulation of voltage source converter based high voltage direct current  
 77 system [29], LFC of power systems with high wind energy penetration [30], position and velocity profile  
 78 tracking control for next-generation servo track writing [31], etc. In addition, a derivative-free nonlinear  
 79 Kalman filter was redesigned as a disturbance observer to estimate additive input disturbances to DFIG,  
 80 which are finally compensated by a feedback controller that enables the generator's state variables to  
 81 track desirable setpoints [32].

82 This paper proposes a perturbation observer based sliding-mode control (POSMC) of DFIG for opti-  
 83 mal power extraction, which novelty and contribution can be summarized as the following four points:

- 84 • The combinatorial effect of wind turbine nonlinearities, generator parameter uncertainties, and wind  
 85 speed randomness is simultaneously estimated online by a sliding-mode state and perturbation observer  
 86 (SMSPO), which is then fully compensated by a robust sliding-mode controller. Thus no accurate system  
 87 model is needed. In contrast, other nonlinear approaches need an accurate system model [11] or can mere-  
 88 ly handle some specific uncertainties, e.g., wind speed uncertainties [15] or parameter uncertainties [16];
- 89 • Only the measurement of rotor speed and reactive power is required by POSMC, while various gener-  
 90 ator variables and parameters are required by references [12, 14]. Hence POSMC is relatively easy to be  
 91 implemented in practice;
- 92 • Compared to other SMC schemes [22, 23], as the upper bound of perturbation is replaced by its real-time  
 93 estimate, the inherent over-conservativeness of SMC can be avoided by the proposed method;
- 94 • POSMC employs a nonlinear SMSPO to estimate the perturbation, which does not have the malignant  
 95 effect of peaking phenomenon existed in HGSPPO [24], Moreover, its structure is simpler than that of

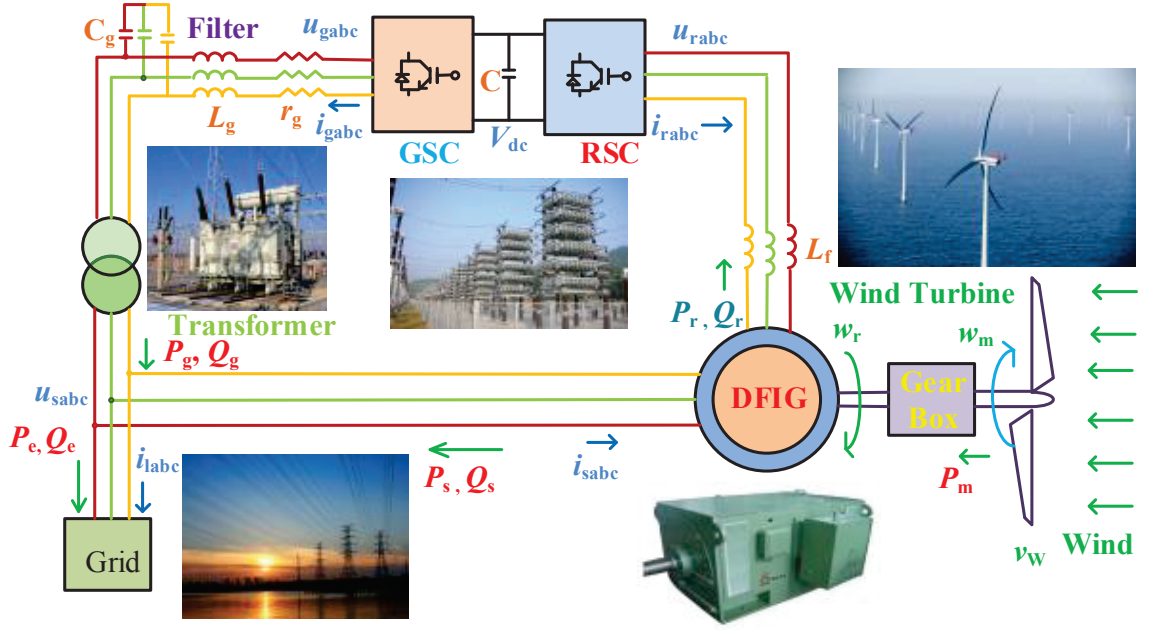


Figure 1: The configuration of a DFIG connected to the power grid.

96 another typical nonlinear observer called ADRC [25].

97 Four case studies have been undertaken to evaluate the effectiveness of the proposed approaches  
 98 and compare its control performance against other typical methods, such as VC, FLC, and SMC. The  
 99 remaining of this paper is organized as follows: Section II is devoted for DFIG modelling while Section III  
 100 develops the POSMC scheme. In Section IV, the POSMC design of DFIG for optimal power extraction is  
 101 investigated. Section V provides the simulation results. Lastly, some concluding remarks are summarized  
 102 in Section VI.

## 103 2 DFIG Modelling

104 A schematic diagram of DFIG connected to a power grid is illustrated in Fig. 1, in which the wind  
 105 turbine is connected to an induction generator through a mechanical shaft system, while the stator is  
 106 directly connected to the power grid and the rotor is fed through a back-to-back converter [7].

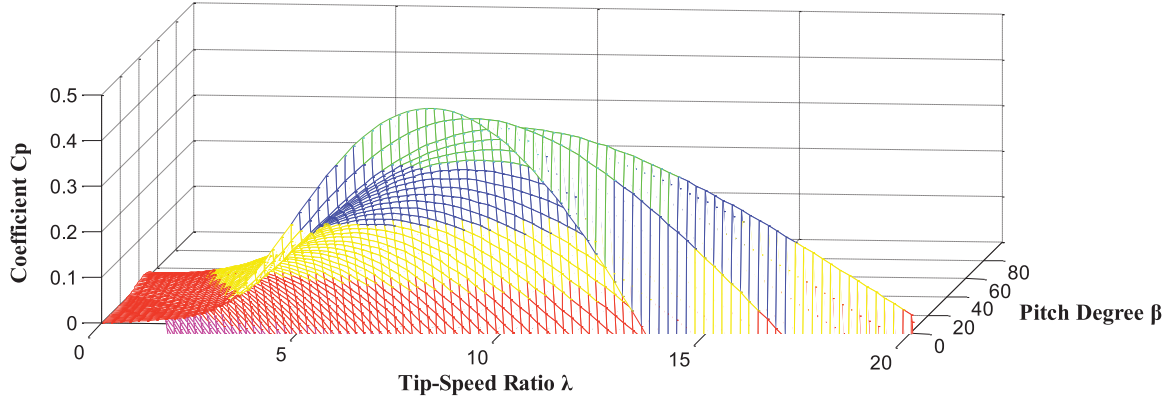


Figure 2: The power coefficient curve  $C_p(\lambda, \beta)$  against tip-speed-ratio  $\lambda$  and blade pitch angle  $\beta$ .

## 2.1 Wind turbine

The aerodynamics of wind turbine can be generically characterized by the power coefficient  $C_p(\lambda, \beta)$ , which is a function of both tip-speed-ratio  $\lambda$  and blade pitch angle  $\beta$ , in which  $\lambda$  is defined by

$$\lambda = \frac{\omega_m R}{v_{\text{wind}}} \quad (1)$$

where  $R$  is the blade radius,  $\omega_m$  is the wind turbine rotational speed and  $v_{\text{wind}}$  is the wind speed. Based on the wind turbine characteristics, a generic equation employed to model  $C_p(\lambda, \beta)$  can be written as [33]

$$C_p(\lambda, \beta) = c_1 \left( \frac{c_2}{\lambda_i} - c_3 \beta - c_4 \right) e^{-\frac{c_5}{\lambda_i}} + c_6 \lambda \quad (2)$$

with

$$\frac{1}{\lambda_i} = \frac{1}{\lambda + 0.08\beta} - \frac{0.035}{\beta^3 + 1} \quad (3)$$

The coefficients  $c_1$  to  $c_6$  are chosen as  $c_1=0.5176$ ,  $c_2=116$ ,  $c_3=0.4$ ,  $c_4=5$ ,  $c_5=21$  and  $c_6=0.0068$  [34]. Particularly, Fig. 2 demonstrates the power coefficient curve  $C_p(\lambda, \beta)$  against tip-speed-ratio  $\lambda$  and blade pitch angle  $\beta$ . Note that this paper adopts a simple wind turbine which blade pitch angle  $\beta$  is a constant as a simplification of wind turbine modelling [35].

The mechanical power that wind turbine can extract from the wind is calculated by

$$P_m = \frac{1}{2} \rho \pi R^2 C_p(\lambda, \beta) v_{\text{wind}}^3 \quad (4)$$

where  $\rho$  is the air density. In the MPPT, the wind turbine always operates under the sub-rated wind speed, in which the aim of controller is to track the optimal active power curve which is obtained by

120 connecting each maximum power point at various wind speed. Under such circumstance, the pitch angle  
 121 control system is deactivated thus  $\beta \equiv 0$  [36]. When the wind speed is beyond the rated value, then the  
 122 control objective will be changed to control the pitch angle, in which the value of pitch angle  $\beta$  will be a  
 123 variable and tuned in the real-time [37].

## 124 2.2 Doubly-fed induction generator

The generator dynamics are described as follows [7, 11, 33]:

$$\frac{di_{qs}}{dt} = \frac{\omega_b}{L'_s} \left( -R_1 i_{qs} + \omega_s L'_s i_{ds} + \frac{\omega_r}{\omega_s} e'_{qs} - \frac{1}{T_r \omega_s} e'_{ds} - v_{qs} + \frac{L_m}{L_{rr}} v_{qr} \right) \quad (5)$$

$$\frac{di_{ds}}{dt} = \frac{\omega_b}{L'_s} \left( -\omega_s L'_s i_{qs} - R_1 i_{ds} + \frac{1}{T_r \omega_s} e'_{qs} + \frac{\omega_r}{\omega_s} e'_{ds} - v_{ds} + \frac{L_m}{L_{rr}} v_{dr} \right) \quad (6)$$

$$\frac{de'_{qs}}{dt} = \omega_b \omega_s \left[ R_2 i_{ds} - \frac{1}{T_r \omega_s} e'_{qs} + \left( 1 - \frac{\omega_r}{\omega_s} \right) e'_{ds} - \frac{L_m}{L_{rr}} v_{dr} \right] \quad (7)$$

$$\frac{de'_{ds}}{dt} = \omega_b \omega_s \left[ -R_2 i_{qs} - \left( 1 - \frac{\omega_r}{\omega_s} \right) e'_{qs} - \frac{1}{T_r \omega_s} e'_{ds} + \frac{L_m}{L_{rr}} v_{qr} \right] \quad (8)$$

125 where  $\omega_b$  is the electrical base speed and  $\omega_s$  is the synchronous angular speed;  $e'_{ds}$  and  $e'_{qs}$  are equivalent  
 126 d-axis and q-axis (dq-) internal voltages;  $i_{ds}$  and  $i_{qs}$  are dq- stator currents;  $v_{ds}$  and  $v_{qs}$  are dq- stator  
 127 terminal voltages;  $v_{dr}$  and  $v_{qr}$  are dq- rotor voltages, respectively. The remained parameters are covered  
 128 in Appendix.

The active power  $P_e$  produced by the generator can be calculated by

$$P_e = e'_{qs} i_{qs} + e'_{ds} i_{ds} \quad (9)$$

Here, the q-axis is aligned with stator voltage while the d-axis leads the q-axis. Thus, one can directly  
 obtain that  $v_{ds} \equiv 0$  and  $v_{qs}$  equals to the magnitude of the terminal voltage. Finally, the reactive power  
 $Q_s$  is given by

$$Q_s = v_{qs} i_{ds} - v_{ds} i_{qs} = v_{qs} i_{ds} \quad (10)$$

## 129 2.3 Shaft system

The shaft system is simply modelled as a single lumped-mass system with a lumped inertia constant denoted as  $H_m$ , calculated by [34].

$$H_m = H_t + H_g \quad (11)$$

130 where  $H_t$  and  $H_g$  are the inertia constants of the wind turbine and the generator, respectively.

131 The electromechanical dynamics is then written by

$$\frac{d\omega_m}{dt} = \frac{1}{2H_m} (T_m - T_e - D\omega_m) \quad (12)$$

132 where  $\omega_m$  is the rotational speed of the lumped-mass system which equals to the generator rotor speed

133  $\omega_r$  when both of them are given in per unit (p.u.);  $D$  represents the damping of the lumped system; and

134  $T_m$  denotes the mechanical torque given as  $T_m = P_m/\omega_m$ , respectively.

## 135 3 Perturbation Observer based Sliding-mode Control

136 Consider an uncertain nonlinear system which has the following canonical form

$$\begin{cases} \dot{x} = Ax + B(a(x) + b(x)u + d(t)) \\ y = x_1 \end{cases} \quad (13)$$

137 where  $x = [x_1, x_2, \dots, x_n]^T \in \mathbb{R}^n$  is the state variable vector;  $u \in \mathbb{R}$  and  $y \in \mathbb{R}$  are the control input and

138 system output, respectively;  $a(x) : \mathbb{R}^n \mapsto \mathbb{R}$  and  $b(x) : \mathbb{R}^n \mapsto \mathbb{R}$  are unknown smooth functions; and  $d(t)$

139  $: \mathbb{R}^+ \mapsto \mathbb{R}$  represents a time-varying external disturbance. The  $n \times n$  matrix  $A$  and  $n \times 1$  matrix  $B$  are

140 of the canonical form as follows

$$A = \begin{bmatrix} 0 & 1 & 0 & \cdots & 0 \\ 0 & 0 & 1 & \cdots & 0 \\ \vdots & & & & \vdots \\ 0 & 0 & 0 & \cdots & 1 \\ 0 & 0 & 0 & \cdots & 0 \end{bmatrix}_{n \times n}, \quad B = \begin{bmatrix} 0 \\ 0 \\ \vdots \\ 0 \\ 1 \end{bmatrix}_{n \times 1} \quad (14)$$

141 The perturbation of system (13) is defined as [24]

$$\Psi(x, u, t) = a(x) + (b(x) - b_0)u + d(t) \quad (15)$$

142 where  $b_0$  is the constant control gain.

143 From the original system (13), the last state  $x_n$  can be rewritten in the presence of perturbation (15),  
144 which yields

$$\dot{x}_n = a(x) + (b(x) - b_0)u + d(t) + b_0u = \Psi(x, u, t) + b_0u \quad (16)$$

145 Define an extended state  $x_{n+1} = \Psi(x, u, t)$ . Then, system (13) can be directly extended into

$$\begin{cases} y = x_1 \\ \dot{x}_1 = x_2 \\ \vdots \\ \dot{x}_n = x_{n+1} + b_0u \\ \dot{x}_{n+1} = \dot{\Psi}(\cdot) \end{cases} \quad (17)$$

146 The new state vector becomes  $x_e = [x_1, x_2, \dots, x_n, x_{n+1}]^T$ , and the following three assumptions are made

- 147 • A.1  $b_0$  is chosen to satisfy:  $|b(x)/b_0 - 1| \leq \theta < 1$ , where  $\theta$  is a positive constant.
- 148 • A.2 The functions  $\Psi(x, u, t) : \mathbb{R}^n \times \mathbb{R} \times \mathbb{R}^+ \mapsto \mathbb{R}$  and  $\dot{\Psi}(x, u, t) : \mathbb{R}^n \times \mathbb{R} \times \mathbb{R}^+ \mapsto \mathbb{R}$  are bounded  
149 over the domain of interest:  $|\Psi(x, u, t)| \leq \gamma_1$ ,  $|\dot{\Psi}(x, u, t)| \leq \gamma_2$  with  $\Psi(0, 0, 0) = 0$  and  $\dot{\Psi}(0, 0, 0) = 0$ ,  
150 where  $\gamma_1$  and  $\gamma_2$  are positive constants.
- 151 • A.3 The desired trajectory  $y_d$  and its up to  $n$ th-order derivative are all continuous and bounded.

152 Here, Assumptions A.1 and A.2 ensure the closed-loop system stability with perturbation estimation,  
153 while assumption A.3 guarantees POSMC can drive the system state  $x$  to track a desired trajectory  
154  $x_d = [y_d, y_d^{(1)}, \dots, y_d^{(n-1)}]^T$ .

155 Throughout this paper,  $\tilde{x} = x - \hat{x}$  refers to the estimation error of  $x$  whereas  $\hat{x}$  represents the estimate  
156 of  $x$ . In the consideration of the worst case, e.g.,  $y = x_1$  is the only measurable state, an  $(n+1)$ th-  
157 order SMSPO for the extended system (17) is designed to simultaneously estimate the system states and

158 perturbation, shown as follows

$$\begin{cases} \dot{\hat{x}}_1 = \hat{x}_2 + \alpha_1 \tilde{x}_1 + k_1 \text{sat}(\tilde{x}_1, \epsilon_o) \\ \vdots \\ \dot{\hat{x}}_n = \hat{\Psi}(\cdot) + \alpha_n \tilde{x}_1 + k_n \text{sat}(\tilde{x}_1, \epsilon_o) + b_0 u \\ \dot{\hat{\Psi}}(\cdot) = \alpha_{n+1} \tilde{x}_1 + k_{n+1} \text{sat}(\tilde{x}_1, \epsilon_o) \end{cases} \quad (18)$$

where  $\alpha_i$ ,  $i = 1, 2, \dots, n+1$ , are the Luenberger observer constants which are chosen to place the poles of  $s^{n+1} + \alpha_1 s^n + \alpha_2 s^{n-1} + \dots + \alpha_{n+1} = (s + \lambda_\alpha)^{n+1} = 0$  being in the open left-half complex plane at  $-\lambda_\alpha$ , with

$$\alpha_i = C_{n+1}^i \lambda_\alpha^i, \quad i = 1, 2, \dots, n+1. \quad (19)$$

159 where  $C_{n+1}^i = \frac{(n+1)!}{i!(n+1-i)!}$ .

In addition, positive constants  $k_i$  are the sliding surface constants, in which

$$k_1 \geq |\tilde{x}_2|_{\max} \quad (20)$$

where the ratio  $k_i/k_1$  ( $i = 2, 3, \dots, n+1$ ) are chosen to put the poles of  $p^n + (k_2/k_1)p^{n-1} + \dots + (k_n/k_1)p + (k_{n+1}/k_1) = (p + \lambda_k)^n = 0$  to be in the open left-half complex plane at  $-\lambda_k$ , yields

$$\frac{k_{i+1}}{k_1} = C_n^i \lambda_k^i, \quad i = 1, 2, \dots, n. \quad (21)$$

160 where  $C_n^i = \frac{n!}{i!(n-i)!}$ .

161 Moreover,  $\text{sat}(\tilde{x}_1, \epsilon_o)$  function is employed to replace conventional  $\text{sgn}(\tilde{x}_1)$  function, such that the  
162 malignant effect of chattering in SMSPO resulted from discontinuity can be reduced, which is defined as  
163  $\text{sat}(\tilde{x}_1, \epsilon_o) = \tilde{x}_1/|\tilde{x}_1|$  when  $|\tilde{x}_1| > \epsilon_o$  and  $\text{sat}(\tilde{x}_1, \epsilon_o) = \tilde{x}_1/\epsilon_o$  when  $|\tilde{x}_1| \leq \epsilon_o$ . In addition,  $\epsilon_o$  denotes the  
164 observer thickness layer boundary.

165 Define an estimated sliding surface as

$$\hat{S}(x, t) = \sum_{i=1}^n \rho_i (\hat{x}_i - y_d^{(i-1)}) \quad (22)$$

166 where the estimated sliding surface gains  $\rho_i = C_{n-1}^{i-1} \lambda_c^{n-i}$ ,  $i = 1, \dots, n$ , place all poles of the estimated  
167 sliding surface at  $-\lambda_c$ , where  $\lambda_c > 0$ .

168 The POSMC for system (13) is designed as

$$u = \frac{1}{b_0} \left[ y_d^{(n)} - \sum_{i=1}^{n-1} \rho_i (\hat{x}_{i+1} - y_d^{(i)}) - \zeta \hat{S} - \varphi \text{sat}(\hat{S}, \epsilon_c) - \hat{\Psi}(\cdot) \right] \quad (23)$$

169 where  $\zeta$  and  $\varphi$  are control gains which are chosen to fulfill the attractiveness of the estimated sliding  
170 surface  $\hat{S}$ . In addition,  $\epsilon_c$  is the controller thickness layer boundary.

## 171 4 POSMC Design of DFIG for Optimal Power Extraction

172 This paper aims to apply POSMC on the rotor-side converter (RSC) of DFIG for an MPPT, while the  
173 dynamics of the grid-side converter (GSC) is ignored. The maximum power point (MPP) is defined as  
174 an operating point of the wind turbine at which maximum mechanical power can be extracted from the  
175 wind turbine [11].

176 Choose the tracking error  $e = [e_1 \ e_2]^T$  of rotor speed  $\omega_r$  and stator reactive power  $Q_s$  as the outputs,  
177 yields

$$\begin{cases} e_1 = \omega_r - \omega_r^* \\ e_2 = Q_s - Q_s^* \end{cases} \quad (24)$$

178 where rotor speed reference  $\omega_r^* = \lambda_{\text{opt}} v_{\text{wind}} / R$  and  $Q_s^*$  denotes the reactive power reference. Differentiate  
179 the tracking error (24) until control inputs  $v_{\text{dr}}$  and  $v_{\text{qr}}$  appeared explicitly, obtains

$$\begin{bmatrix} \ddot{e}_1 \\ \ddot{e}_2 \end{bmatrix} = \begin{bmatrix} f_1 & - & \ddot{\omega}_r^* \\ f_2 & - & \dot{Q}_s^* \end{bmatrix} + B \begin{bmatrix} v_{\text{dr}} \\ v_{\text{qr}} \end{bmatrix} \quad (25)$$

180 where

$$f_1 = \frac{T_m}{2H_m} - \frac{1}{2H_m} \left\{ w_b \left[ \left( 1 - \frac{\omega_r}{\omega_s} \right) (e'_{\text{ds}} i_{\text{qs}} - e'_{\text{qs}} i_{\text{ds}}) - \frac{1}{\omega_s T_r} (e'_{\text{qs}} i_{\text{qs}} + e'_{\text{ds}} i_{\text{ds}}) \right] + \frac{\omega_b}{\omega_s L'_s} \left[ \frac{\omega_r}{\omega_s} (e'^2_{\text{ds}} + e'^2_{\text{qs}}) \right. \right. \\ \left. \left. + \omega_s L'_s (e'_{\text{qs}} i_{\text{ds}} - e'_{\text{ds}} i_{\text{qs}}) - R_1 (e'_{\text{qs}} i_{\text{qs}} + e'_{\text{ds}} i_{\text{ds}}) - e'_{\text{qs}} v_{\text{qs}} - e'_{\text{ds}} v_{\text{ds}} \right] \right\} \quad (26)$$

181

$$f_2 = \frac{\omega_b}{L'_s} \left( \omega_s L'_s i_{\text{qs}} + R_1 i_{\text{ds}} - \frac{1}{\omega_s T_r} e'_{\text{qs}} - \frac{\omega_r}{\omega_s} e'_{\text{ds}} \right) v_{\text{qs}} + \frac{\omega_b}{L'_s} \left( -R_1 i_{\text{qs}} + \omega_s L'_s i_{\text{ds}} + \frac{\omega_r}{\omega_s} e'_{\text{qs}} - \frac{1}{\omega_s T_r} e'_{\text{ds}} - v_{\text{qs}} \right) v_{\text{ds}} \quad (27)$$

182 and

$$B = \begin{bmatrix} \frac{\omega_b L_m}{-2H_m L_{rr}} \left( \frac{e'_{\text{ds}}}{\omega_s L'_s} - i_{\text{qs}} \right) & \frac{\omega_b L_m}{-2H_m L_{rr}} \left( \frac{e'_{\text{qs}}}{\omega_s L'_s} + i_{\text{ds}} \right) \\ -\frac{\omega_b L_m}{L'_s L_{rr}} v_{\text{qs}} & \frac{\omega_b L_m}{L'_s L_{rr}} v_{\text{ds}} \end{bmatrix} \quad (28)$$

183 where  $B$  is the control gain matrix. As  $\det(B) = -\frac{\omega_b^2 L_m^2 v_{qs}}{2H_m L_s^2 L_r^2} (\frac{e'_{qs}}{\omega_s L_s} + i_{ds}) \neq 0$ , it is invertible and the  
 184 transformed system is linearizable over the whole operation range.

The time derivative of  $T_m$  in Eq. (26) is calculated by

$$\dot{T}_m = \frac{\partial T_m}{\partial \omega_r} \times \frac{d\omega_r}{dt} + \frac{\partial T_m}{\partial v_{\text{wind}}} \times \frac{dv_{\text{wind}}}{dt} \quad (29)$$

where

$$\frac{\partial T_m}{\partial \omega_r} = \frac{1}{2} \rho A v_{\text{wind}}^3 \left\{ c_1 e^{-c_5 (\frac{v_{\text{wind}}}{R\omega_r} - 0.035)} \left[ \frac{c_2 c_5 v_{\text{wind}}^2}{R^2 \omega_r^4} - \frac{(2c_2 + 0.035c_2 c_5 + c_4 c_5) v_{\text{wind}}}{R \omega_r^3} + \frac{0.035c_2 + c_4}{\omega_r^2} \right] \right\} \quad (30)$$

$$\frac{\partial T_m}{\partial v_{\text{wind}}} = \frac{1}{2} \rho A v_{\text{wind}}^2 \left\{ c_1 e^{-c_5 (\frac{v_{\text{wind}}}{R\omega_r} - 0.035)} \left[ -\frac{c_2 c_5 v_{\text{wind}}^2}{R^2 \omega_r^3} + \frac{(4c_2 + 0.035c_2 c_5 + c_4 c_5) v_{\text{wind}}}{R \omega_r^2} - \frac{0.105c_2 + 3c_4}{\omega_r} \right] \right\} \quad (31)$$

$$\left. - \frac{2c_6 R}{v_{\text{wind}}} \right\}$$

185 Assume all the nonlinearities are unknown, define the perturbations  $\Psi_1(\cdot)$  and  $\Psi_2(\cdot)$  for system (25)

186 as

$$\begin{bmatrix} \Psi_1(\cdot) \\ \Psi_2(\cdot) \end{bmatrix} = \begin{bmatrix} f_1 \\ f_2 \end{bmatrix} + (B - B_0) \begin{bmatrix} v_{\text{dr}} \\ v_{\text{qr}} \end{bmatrix} \quad (32)$$

187 where the constant control gain  $B_0$  is given by

$$B_0 = \begin{bmatrix} b_{11} & 0 \\ 0 & b_{22} \end{bmatrix} \quad (33)$$

188 Then system (25) can be rewritten as

$$\begin{bmatrix} \dot{e}_1 \\ \dot{e}_2 \end{bmatrix} = \begin{bmatrix} \Psi_1(\cdot) \\ \Psi_2(\cdot) \end{bmatrix} + B_0 \begin{bmatrix} v_{\text{dr}} \\ v_{\text{qr}} \end{bmatrix} - \begin{bmatrix} \dot{\omega}_r^* \\ Q_s^* \end{bmatrix} \quad (34)$$

189 Define  $z_{11} = \omega_r$  and  $z_{12} = \dot{z}_{11}$ , a third-order SMSPO is adopted to estimate  $\Psi_1(\cdot)$  as

$$\begin{cases} \dot{\hat{z}}_{11} = \hat{z}_{12} + \alpha_{11} \tilde{\omega}_r + k_{11} \text{sat}(\tilde{\omega}_r, \epsilon_o) \\ \dot{\hat{z}}_{12} = \hat{\Psi}_1(\cdot) + \alpha_{12} \tilde{\omega}_r + k_{12} \text{sat}(\tilde{\omega}_r, \epsilon_o) + b_{11} v_{\text{dr}} \\ \dot{\hat{\Psi}}_1(\cdot) = \alpha_{13} \tilde{\omega}_r + k_{13} \text{sat}(\tilde{\omega}_r, \epsilon_o) \end{cases} \quad (35)$$

190 where observer gains  $k_{11}$ ,  $k_{12}$ ,  $k_{13}$ ,  $\alpha_{11}$ ,  $\alpha_{12}$ , and  $\alpha_{13}$ , are all positive constants.

191 Define  $z_{21} = Q_s$ , a second-order sliding-mode perturbation observer (SMPO) is employed to estimate  
 192  $\Psi_2(\cdot)$  as

$$\begin{cases} \dot{\hat{z}}_{21} = \hat{\Psi}_2(\cdot) + \alpha_{21}\tilde{Q}_s + k_{21}\text{sat}(\tilde{Q}_s, \epsilon_o) + b_{22}v_{qr} \\ \dot{\hat{\Psi}}_2(\cdot) = \alpha_{22}\tilde{Q}_s + k_{22}\text{sat}(\tilde{Q}_s, \epsilon_o) \end{cases} \quad (36)$$

193 where observer gains  $k_{21}$ ,  $k_{22}$ ,  $\alpha_{21}$ , and  $\alpha_{22}$ , are all positive constants.

194 The estimated sliding surface of system (25) is chosen by

$$\begin{bmatrix} \hat{S}_1 \\ \hat{S}_2 \end{bmatrix} = \begin{bmatrix} \rho_1(\hat{z}_{11} - \omega_r^*) + \rho_2(\hat{z}_{12} - \dot{\omega}_r^*) \\ \hat{z}_{21} - Q_s^* \end{bmatrix} \quad (37)$$

195 where  $\rho_1$  and  $\rho_2$  are the positive sliding surface gains. The attractiveness of the estimated sliding surface  
 196 (37) ensures rotor speed  $\omega_r$  and reactive power  $Q_s$  can effectively track to their reference.

197 The POSMC of system (25) is designed as

$$\begin{bmatrix} v_{dr} \\ v_{qr} \end{bmatrix} = B_0^{-1} \begin{bmatrix} \ddot{\omega}_r^* - \rho_1(\hat{z}_{12} - \dot{\omega}_r^*) - \zeta_1\hat{S}_1 - \varphi_1\text{sat}(\hat{S}_1, \epsilon_c) - \hat{\Psi}_1(\cdot) \\ \dot{Q}_s^* - \zeta_2\hat{S}_2 - \varphi_2\text{sat}(\hat{S}_2, \epsilon_c) - \hat{\Psi}_2(\cdot) \end{bmatrix} \quad (38)$$

198 where positive control gains  $\zeta_1$ ,  $\zeta_2$ ,  $\varphi_1$ , and  $\varphi_2$  are chosen to guarantee the convergence of system (25).

199 During the most severe disturbance, both the rotor speed and reactive power may reduce from their  
 200 initial value to around zero within a short period of time  $\Delta$ . Thus the boundary values of the state  
 201 and perturbation estimates can be calculated by  $|\hat{z}_{11}| \leq |\omega_r^*|$ ,  $|\hat{z}_{12}| \leq |\omega_r^*|/\Delta$ , and  $|\hat{\Psi}_1(\cdot)| \leq |\omega_r^*|/\Delta^2$ ,  
 202  $|\hat{z}_{21}| \leq |Q_s^*|$ , and  $|\hat{\Psi}_2(\cdot)| \leq |Q_s^*|/\Delta$ , respectively. Note that the selection of  $B_0$  (33) fully decouples system  
 203 (25) into two single-input single-output (SISO) systems (34). As a consequence, control inputs  $v_{dr}$  and  
 204  $v_{qr}$  can independently regulate rotor speed  $\omega_r$  and reactive power  $Q_s$ .

205 To this end, the overall POSMC structure of DFIG is illustrated by Fig. 3, in which only the  
 206 measurement of rotor speed  $\omega_r$  and reactive power  $Q_s$  at the RSC side is required. Moreover, one can  
 207 readily find from Fig. 3 that POSMC has an integrated structure which does not need any auxiliary  
 208 dq-axis current regulation loops that usually required by VC [3]. At last, the obtained control inputs  
 209 (38) are modulated by the sinusoidal pulse width modulation (SPWM) technique [38].

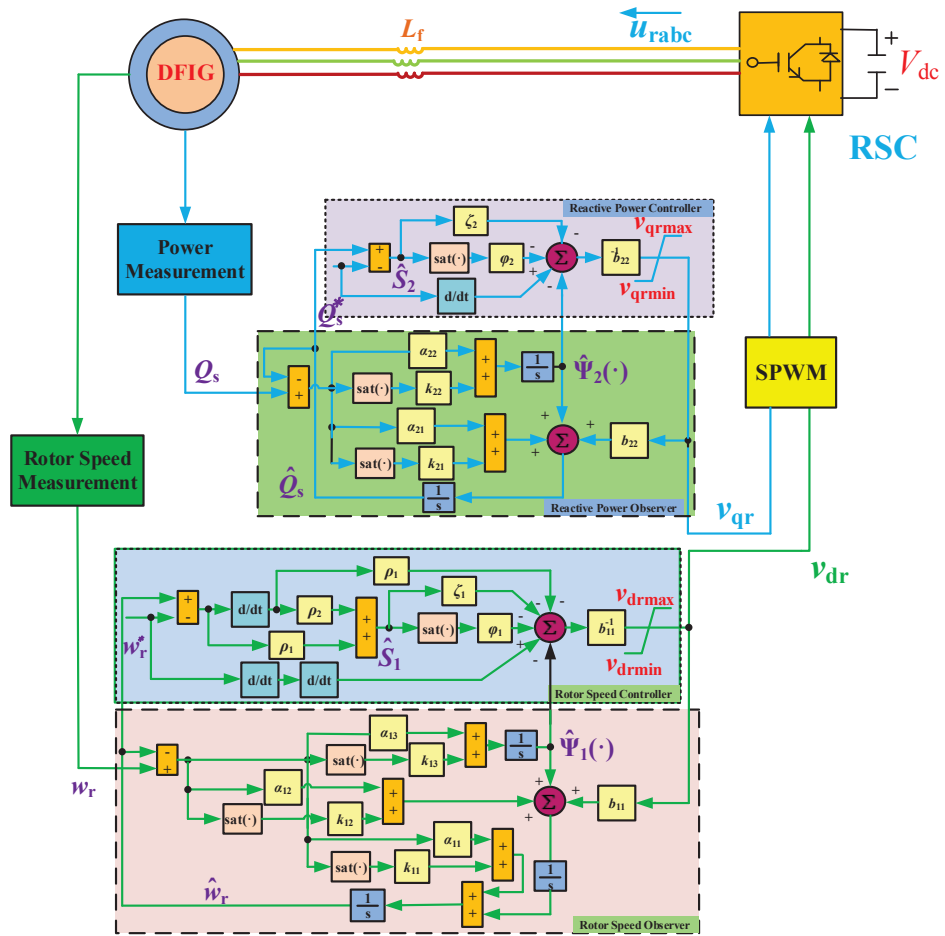


Figure 3: The overall POSMC structure of DFIG.

## 5 Case Studies

The proposed POSMC has been applied to achieve an MPPT of a DFIG connected to the power grid, which control performance is compared to that of conventional VC [3], FLC [11], SMC [20], under four cases, i.e., step change of wind speed, random wind speed variation, FRT capability, and system robustness against parameter uncertainties. Since the control inputs might exceed the admissible capacity of RSC at some operation point, their values must be limited. Here,  $v_{dr}$  and  $v_{qr}$  are scaled proportionally as: if  $v_r = \sqrt{v_{dr}^2 + v_{qr}^2} > v_{r\_max}$ , then set  $v_{dr\_lim} = v_{dr}v_{r\_max}/v_r$  and  $v_{qr\_lim} = v_{qr}v_{r\_max}/v_r$  [11], respectively. Besides, the controller parameters are tabulated in Table 1. The simulation is executed on Matlab/Simulink 7.10 using a personal computer with an IntelR CoreTmi7 CPU at 2.2 GHz and 4 GB of RAM.

Table 1: POSMC parameters for the DFIG

rotor controller gains			
$b_{11} = -2500$	$\rho_1 = 750$	$\rho_2 = 1$	$\zeta_1 = 50$
$\varphi_1 = 40$	$\epsilon_o = 0.2$		
rotor observer gains			
$\alpha_{11} = 30$	$\alpha_{12} = 300$	$\alpha_{13} = 1000$	$\Delta = 0.01$
$k_{11} = 20$	$k_{12} = 600$	$k_{13} = 6000$	
reactive power controller gains			
$b_{22} = 6000$	$\zeta_2 = 10$	$\varphi_2 = 10$	$\epsilon_c = 0.2$
reactive power observer gains			
$\alpha_{21} = 40$	$\alpha_{22} = 400$	$k_{21} = 15$	$k_{22} = 600$

### 5.1 Step change of wind speed

A series of four consecutive step changes of wind speed  $v_{wind}=8-12$  m/s are tested, in which a 1 m/s wind speed increase is added during each step change to briefly mimic a gust. The MPPT performance of all controllers is compared in Fig. 4. It shows that POSMC can extract the maximal wind energy with less oscillations, meanwhile it can also regulate the active power and reactive power more rapidly and smoothly compared to that of other algorithms.

### 5.2 Random variation of wind speed

A stochastic wind speed variation is tested to examine the control performance of the proposed approach, which starts from 8 m/s and gradually reaches to 12 m/s, as demonstrated by Fig. 5. The system responses are provided in Fig. 6, from which it can be clearly observed that POSMC is able to achieve the least oscillations of rotor speed error and reactive power thanks to the online perturbation compensation. Additionally, its power coefficient is the closest to the optimum thus the wind energy can be optimally

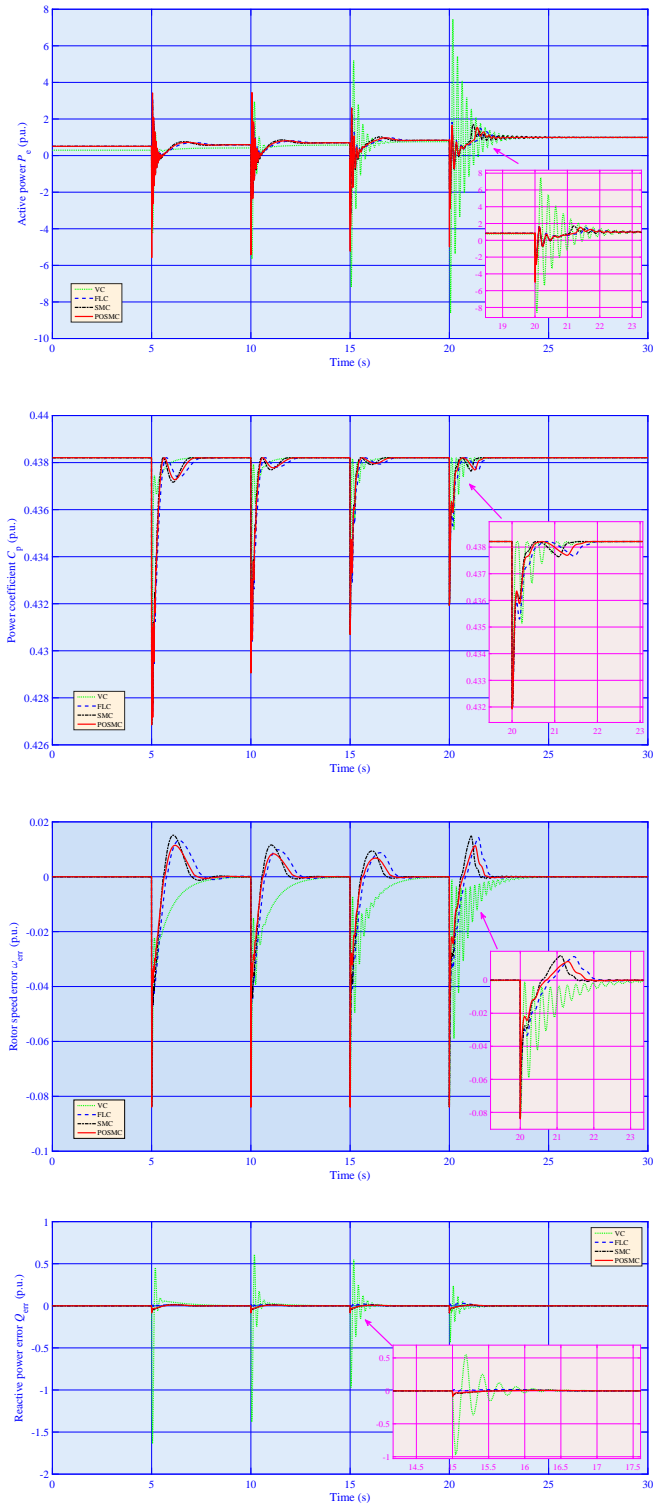


Figure 4: MPPT performance to a series of step change of wind speed from 8 m/s to 12 m/s.

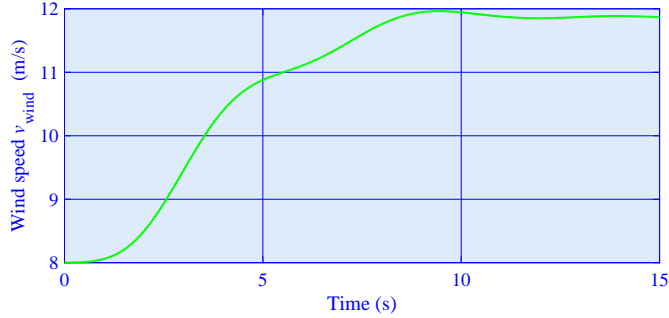


Figure 5: The tested random wind speed variation from 8 m/s to 12 m/s.

231 extracted under random wind speed variations.

### 232 5.3 FRT performance

233 With the rapidly ever-growing integration of WECS into the main power grid, it often requires that  
 234 WECS can realize FRT when the power grid voltage is temporarily reduced due to a fault or a sudden  
 235 load change occurred in the power grid, or can even address the generator to stay operational and not  
 236 disconnect from the power grid during and after the voltage drop [39,40]. A 625 ms voltage dip starting at  
 237  $t=1$  s from nominal value to 0.3 p.u. and restores to 0.9 p.u. is applied [41], while the system responses  
 238 are presented by Fig. 7. One can definitely find that POSMC is able to effectively suppress the power  
 239 oscillations and maintain the largest wind power extraction during FRT, while VC requires the longest  
 240 time to restore the system from such harmful contingencies.

241 Lastly, the estimation performance of perturbation observers during the FRT has also been carefully  
 242 monitored, as shown in Fig. 8. It gives that the perturbations can be rapidly estimated in around 250  
 243 ms while the relative high-frequency oscillations emerged in the initial phase is due to the discontinuity  
 244 of power grid voltage and sliding-mode mechanism caused in perturbation observer loop.

### 245 5.4 System robustness with parameter uncertainties

246 A series of plant-model mismatches of stator resistance  $R_s$  and mutual inductance  $L_m$  with  $\pm 20\%$  un-  
 247 certainties are undertaken to evaluate the robustness of POSMC, in which a 0.25 p.u. voltage drop at  
 248 power grid is tested while the peak value of total active power  $|P_e|$  is recorded for a clear comparison. It  
 249 presents from Fig. 9 that the variation of  $|P_e|$  obtained by POSMC is the smallest among all approach-  
 250 es, i.e., around 2.3% variation of  $|P_e|$  to the stator resistance  $R_s$  and 1.4% variation to that of mutual  
 251 inductance  $L_m$ , respectively. This is because of its elegant merits of the full perturbation compensation

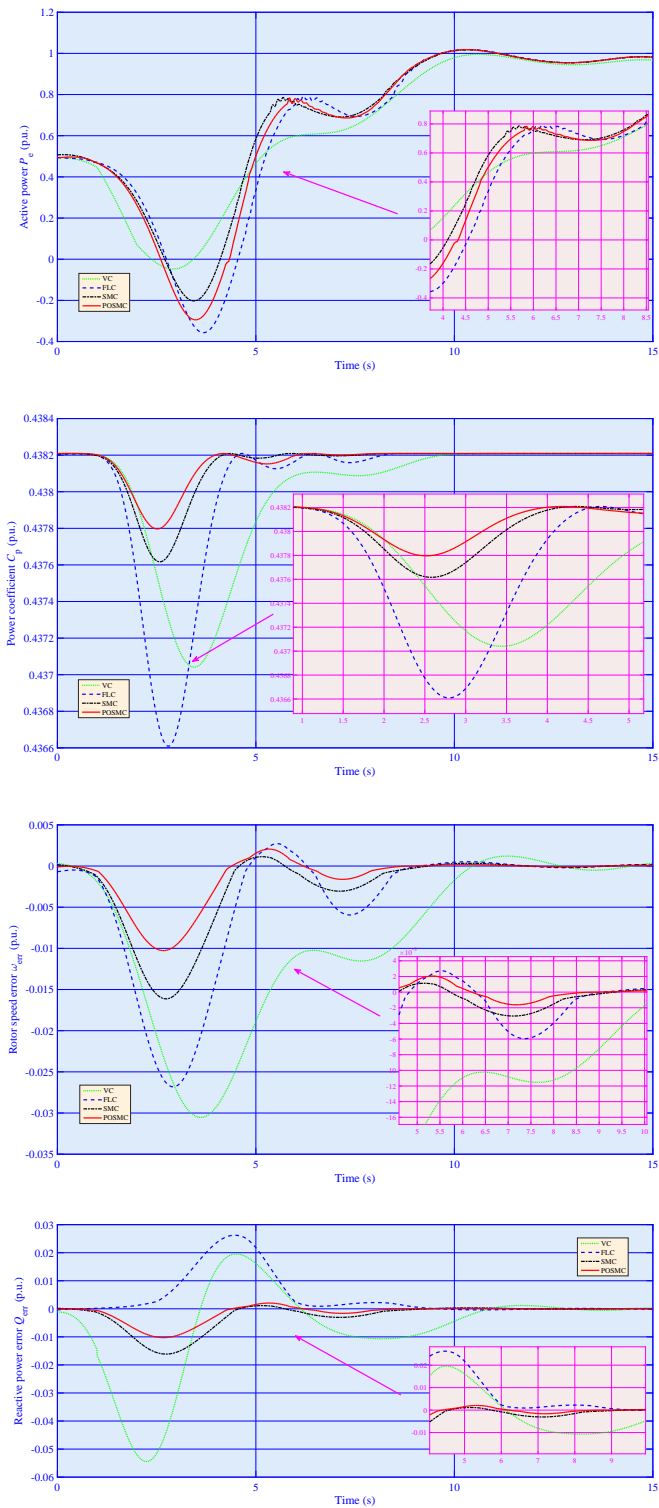


Figure 6: MPPT performance to a random variation of wind speed from 8 m/s to 12 m/s.

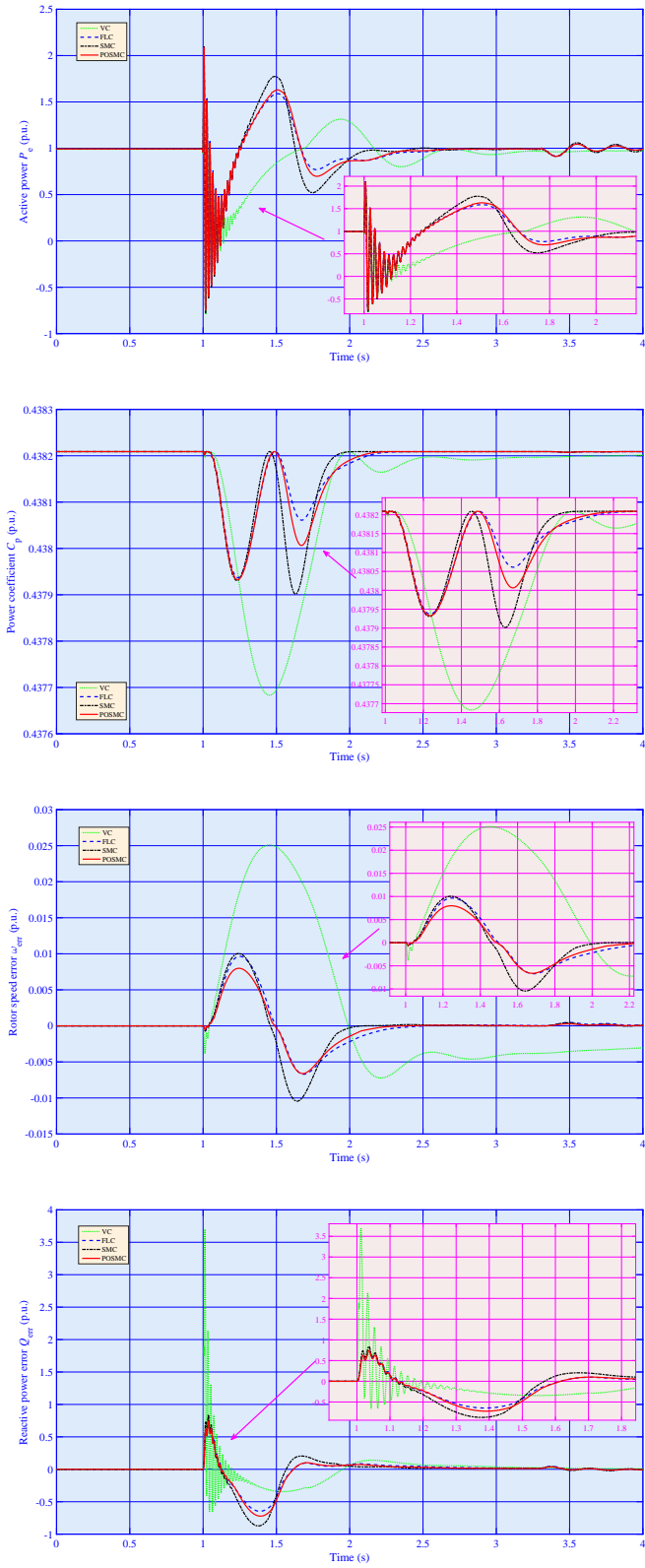


Figure 7: System responses under FRT (a 625 ms voltage dip starting at  $t=1$  s from nominal value to 0.3 p.u. and restores to 0.9 p.u.).

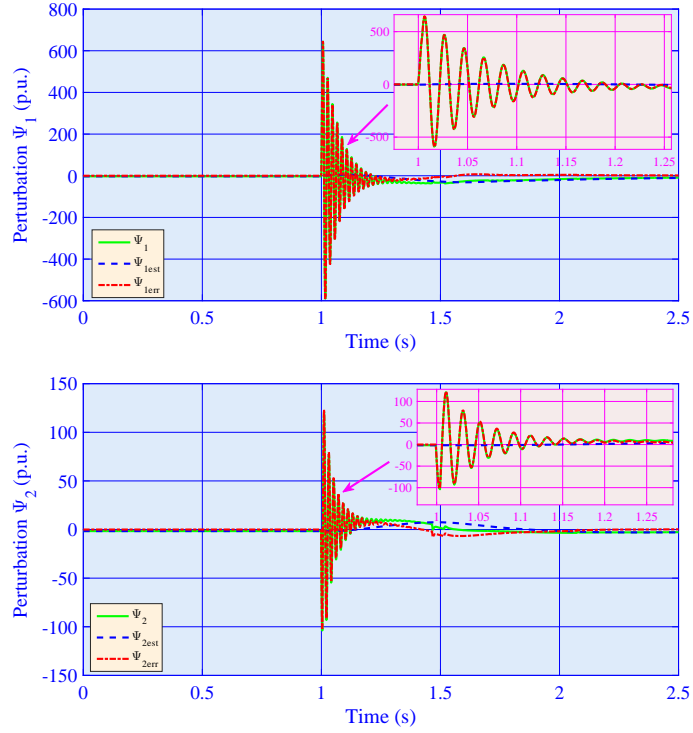


Figure 8: Perturbation estimation performance of SMSPO and SMPO during FRT.

252 and sliding-mode mechanism, such that the greatest robustness can be provided. Obviously, FLC has  
 253 the largest variation against parameter uncertainties as it requires an accurate system model, i.e., around  
 254 19.7% variation of  $|P_e|$  to the stator resistance  $R_s$  and 22.5% variation to that of mutual inductance  $L_m$ ,  
 255 respectively.

Table 2: IAE indices (in p.u.) of different control schemes calculated in different cases

Method \ Case	Step change of wind speed		Random variation of wind speed		Fault-ride through	
	IAE <sub>Q1</sub>	IAE <sub>V<sub>dc1</sub></sub>	IAE <sub>Q1</sub>	IAE <sub>V<sub>dc1</sub></sub>	IAE <sub>Q1</sub>	IAE <sub>V<sub>dc1</sub></sub>
VC	2.18E-02	4.29E-03	4.77E-03	2.36E-03	6.02E-04	5.86E-04
FLC	1.43E-02	3.15E-03	3.79E-03	1.85E-03	3.78E-04	3.23E-04
SMC	1.04E-02	2.87E-03	2.08E-03	9.96E-04	2.54E-04	2.07E-04
POSMC	<b>7.21E-03</b>	<b>1.24E-03</b>	<b>6.97E-04</b>	<b>4.71E-04</b>	<b>1.89E-04</b>	<b>1.21E-04</b>

## 256 5.5 Comparative studies

257 The integral of absolute error (IAE) indices of each approach calculated in different cases are summarized  
 258 in Table 2, where  $IAE_x = \int_0^T |x - x^*| dt$  and  $x^*$  is the reference of variable  $x$ . The simulation time  $T=30$   
 259 s. It shows that POSMC owns the lowest IAE indices (in bold) in all cases compared to those of other

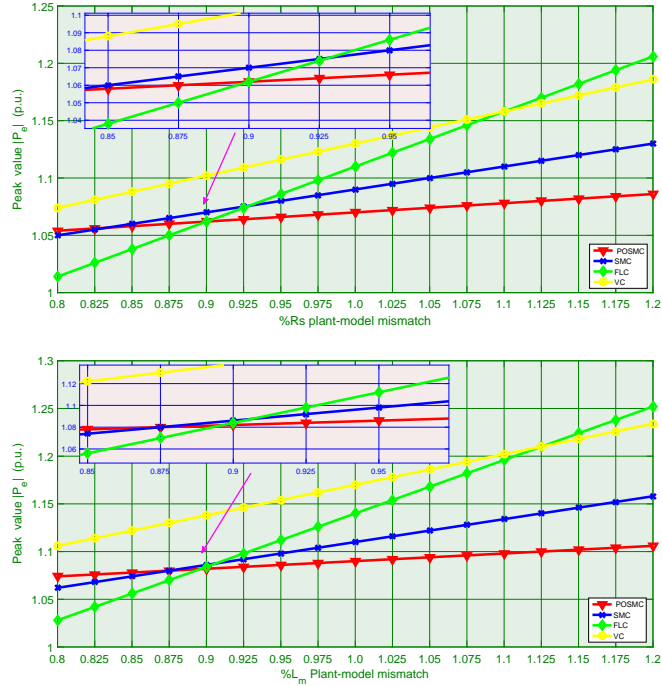


Figure 9: Peak value of active power  $|P_e|$  obtained under a 0.25 p.u. voltage drop at power grid with 20% variation of the stator resistance  $R_s$  and mutual inductance  $L_m$  of different approaches, respectively.

260 methods. In particular, its  $IAE_{Q_1}$  obtained in random variation of wind speed is merely 33.51%, 18.39%,  
 261 and 14.61% to that of SMC, FLC, and VC, respectively; Additionally, its  $IAE_{V_{dc1}}$  obtained in voltage  
 262 drop at power grid is just 58.45%, 37.46%, and 20.65% to that of SMC, FLC, and VC, respectively.

263 The overall control efforts of different controllers needed in three cases are given in Fig. 10. One can  
 264 easily conclude that the overall control efforts of POSMC are the least in all cases except of FRT, this is  
 265 resulted from its merits that the over-conservativeness of control efforts is only involved in the observer  
 266 loop and excluded from the controller loop. Therefore, POSMC outperforms other methods with greater  
 267 robustness enhancement as well as more reasonable control efforts.

## 268 6 Conclusions

269 This paper proposes a robust sliding-mode controller scheme called POSMC to achieve an optimal pow-  
 270 er extraction of DFIG in various operation conditions. A perturbation is firstly defined to aggregate  
 271 the wind turbine nonlinearities, generator parameter uncertainties, and wind speed randomness, which  
 272 is then rapidly estimated by nonlinear perturbation observers and fully compensated by POSMC, so  
 273 that a consistent and robust control performance under different operation conditions can be achieved.

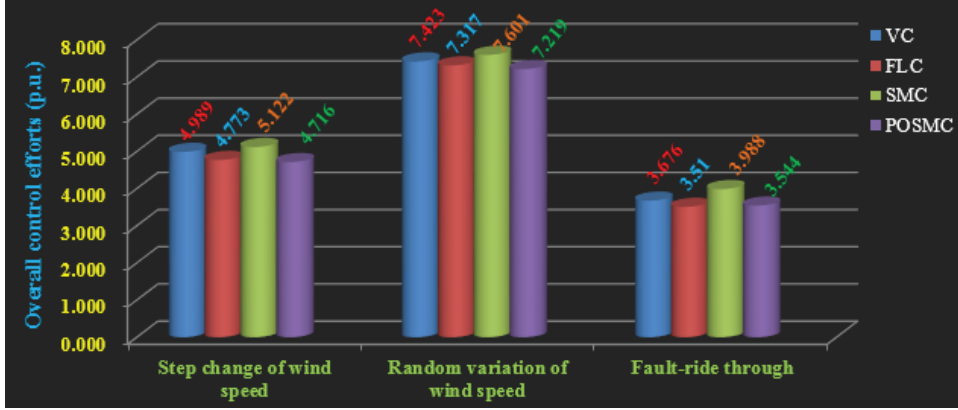


Figure 10: Comparison of control efforts (in p.u.) of different controllers required in three cases.

Simulation results have demonstrated that POSMC can optimally extract the wind energy during wind speed variations and effectively suppress the power oscillations during FRT, together with suitable control efforts thanks to the perturbation compensation.

Compared to other typical nonlinear robust approaches, POSMC can be readily implemented in practice as it only requires the measurement of rotor speed (by an additional rotor speed measuring apparatus) and reactive power (read directly from current power measurement platform), hence the construction costs of measurement apparatus is quite low. Moreover, as POSMC is a decentralized control scheme, no central controller is needed in the face of large-scale wind farms.

## Appendix

System parameters [7, 11, 33]:

$$\omega_b = 100\pi \text{ rad/s}, \omega_s = 1.0 \text{ p.u.}, \omega_{r\_base} = 1.29, v_{s\_nom} = 1.0 \text{ p.u.}$$

DFIG parameters:

$$P_{rated} = 5 \text{ MW}, R_s = 0.005 \text{ p.u.}, R_r = 1.1R_s, L_m = 4.0 \text{ p.u.}, L_{ss} = 1.01L_m, L_{rr} = 1.005L_{ss}, L'_s = L_{ss} - L_m^2/L_{rr}, T_r = L_{rr}/R_r, R_1 = R_s + R_2, R_2 = (L_m/L_{rr})^2R_r.$$

Wind turbine parameters:

$$\rho = 1.225 \text{ kg/m}^3, R = 58.59 \text{ m}^2, v_{wind\_nom} = 12 \text{ m/s}, \lambda_{opt} = 6.325, H_m = 4.4 \text{ s}, D = 0 \text{ p.u.}$$

## Acknowledgements

The authors gratefully acknowledge the support of National Basic Research Program of China (973 Program: 2013CB228205), National Natural Science Foundation of China (51477055, 51667010), Yunnan

293 Provincial Talents Training Program (KKSJ201604044), and Scientific Research Foundation of Yunnan  
294 Provincial Department of Education (KKJB201704007).

## 295 References

- 296 [1] Hooper T., Beaumont N., and Hattam C. ‘The implications of energy systems for ecosystem services:  
297 A detailed case study of offshore wind’, *Renewable and Sustainable Energy Reviews*, 70, 230-241  
298 (2017).
- 299 [2] Matteo M., Riccardo M., Vincenzo D., and Riccardo A. ‘A new model for environmental and  
300 economic evaluation of renewable energy systems: The case of wind turbines’, *Applied Energy*, 189,  
301 739-752 (2017).
- 302 [3] Li S. H., Haskew T. A., Williams K. A., and Swatloski R. P. ‘Control of DFIG wind turbine with  
303 direct-current vector control configuration’, *IEEE Transactions on Sustainable Energy*, 3(1), 1-11  
304 (2012).
- 305 [4] Song D., Yang J., Cai Z., Dong M., Su M., and, Wang Y. ‘Wind estimation with a non-standard  
306 extended Kalman filter and its application on maximum power extraction for variable speed wind  
307 turbines’, *Applied Energy*, 190, 670-685 (2017).
- 308 [5] Gilmanur R. and Mohd H. A., ‘Fault ride through capability improvement of DFIG based wind farm  
309 by fuzzy logic controlled parallel resonance fault current limiter’, *Electric Power Systems Research*,  
310 146, 1-8 (2017).
- 311 [6] Heri S., Arif M., et al. ‘Optimal controller for doubly fed induction generator (DFIG) using differ-  
312 ential evolutionary algorithm (DE)’, *2015 International seminar on intelligent technology and its  
313 applications*, p. 159-164 (2015).
- 314 [7] Yang B., Zhang X. S., Yu T., Shu H. C., and Fang Z. H. ‘Grouped grey wolf optimizer for maximum  
315 power point tracking of doubly-fed induction generator based wind turbine’, *Energy Conversion and  
316 Management*, 133, 427-443 (2017).
- 317 [8] Delgarm N., Sajadi B., Kowsary F., and Delgarm S., ‘Multi-objective optimization of the building  
318 energy performance: A simulation-based approach by means of particle swarm optimization (PSO)’,  
319 *Applied Energy*, 170, 293-303 (2016).

- 320 [9] Wieczorek M. and Lewandowski M. ‘A mathematical representation of an energy management  
321 strategy for hybrid energy storage system in electric vehicle and real time optimization using a  
322 genetic algorithm’, *Applied Energy*, 192, 222-233 (2017).
- 323 [10] Sachez-Lozano J. M., Garcia-Cascales M. S., and Lamata M. T. ‘GIS-based onshore wind farm site  
324 selection using Fuzzy Multi-Criteria Decision Making methods. Evaluating the case of Southeastern  
325 Spain’, *Applied Energy*, 171, 86-102 (2016).
- 326 [11] Yang B., Jiang L., Wang L., Yao W., and Wu Q. H. ‘Nonlinear maximum power point tracking  
327 control and modal analysis of DFIG based wind turbine’, *International Journal of Electrical Power  
328 and Energy Systems*, 74, 429-436 (2016).
- 329 [12] Gayen P. K., Chatterjee D., and Goswami S. K. ‘Stator side active and reactive power control  
330 with improved rotor position and speed estimator of a grid connected DFIG (doubly-fed induction  
331 generator)’, *Energy*, 89, 461-472 (2015).
- 332 [13] Errouissi R., Al-Durra A., Muyeen S. M., Leng S., and Blaabjerg F. ‘Offset-free direct power control  
333 of DFIG under continuous-time model predictive control’, *IEEE Transactions on Power Electronics*,  
334 32(3), 2265-2277 (2017).
- 335 [14] Taveiros F. E. V., Barros L. S., and Costa F. B. ‘Back-to-back converter state-feedback control of  
336 DFIG (doubly-fed induction generator)-based wind turbines’, *Energy*, 89, 896-906 (2015).
- 337 [15] Phan D. C. and Yamamoto S. ‘Rotor speed control of doubly fed induction generator wind turbines  
338 using adaptive maximum power point tracking’, *Energy*, 111, 377-388 (2016).
- 339 [16] Badre B., Mohammed K., Ahmed L., Mohammed T., and Aziz D. ‘Observer backstepping control  
340 of DFIG-Generators for wind turbines variable-speed: FPGA-based implementation’, *Renewable  
341 Energy*, 81, 903-917 (2015).
- 342 [17] Guo W. T., Liu F., Si J., He D., Harley R., and Mei S. W. ‘Approximate dynamic programming  
343 based supplementary reactive power control for DFIG wind farm to enhance power system stability’,  
344 *Neurocomputing*, 170, 417-427 (2015).
- 345 [18] Maissa F., Oscar B., and Lassaad S. ‘A new maximum power point method based on a sliding mode  
346 approach for solar energy harvesting’, *Applied Energy*, 185, 1185-1198 (2017).

- 347 [19] Saad N. H., Sattar A. A., and Mansour A. E. M. ‘Low voltage ride through of doubly-fed induction  
348 generator connected to the grid using sliding mode control strategy’, *Renewable Energy*, 80, 583-594  
349 (2015).
- 350 [20] Benbouzid M., Beltran B., Amirat Y., Yao G., Han J. G., and Mangel H. ‘Second-order slid-  
351 ing mode control for DFIG-based wind turbines fault ride-through capability enhancement’, *ISA*  
352 *Transactions*, 53, 827-833, (2014).
- 353 [21] Soufi Y., Kahla S., and Bechouat M. ‘Particle swarm optimization based sliding mode control  
354 of variable speed wind energy conversion system’, *International Journal of Hydrogen Energy*, 41,  
355 20956-20963 (2016).
- 356 [22] Li S. Z., Wang H. P., Tian Y., Aitouch A., and Klein J. ‘Direct power control of DFIG wind turbine  
357 systems based on an intelligent proportional-integral sliding mode control’, *ISA Transactions*, 64,  
358 431-439 (2016).
- 359 [23] Ebrahimkhani S. ‘Robust fractional order sliding mode control of doubly-fed induction generator  
360 (DFIG)-based wind turbines’, *ISA Transactions*, 63, 343-354 (2016).
- 361 [24] Yang B., Jiang L., Yao W., and Wu Q. H. ‘Perturbation estimation based coordinated adaptive  
362 passive control for multimachine power systems’, *Control Engineering Practice*, 44, 172-192 (2015).
- 363 [25] Tohidi A., Hajieghrary H., and Hsieh M. A. ‘Adaptive disturbance rejection control scheme for  
364 DFIG-based wind turbine: theory and experiments’, *IEEE Transactions on Industry Applications*,  
365 52(3), 2006-2015 (2016).
- 366 [26] Tang Y. M., Bai Y., Huang C. Z., and Du B. ‘Linear active disturbance rejection-based load  
367 frequency control concerning high penetration of wind energy’, *Energy Conversion and Managemen*,  
368 95, 259-271, (2015).
- 369 [27] Liu Y., Wu Q. H., Zhou X. X., and Jiang L. ‘Perturbation observer based multiloop control for the  
370 DFIG-WT in multimachine power system’, *IEEE Transactions on Power Systems*, 29(6), 2905-2915  
371 (2014).
- 372 [28] Zhang J., Liu X., Xia Y., Zuo Z., and Wang Y. ‘Disturbance observer-based integral sliding-mode  
373 control for systems with mismatched disturbances’, *IEEE Transactions on Industrial Electronics*,  
374 63(11), 7040-7048 (2016).

- 375 [29] Yang B., Sang Y. Y., Shi K., Yao W., Jiang L., and Yu T. ‘Design and real-time implementation  
376 of perturbation observer based sliding-mode control for VSC-HVDC systems’, *Control Engineering  
377 Practice*, 56, 13-26 (2016).
- 378 [30] Mi Y., Fu Y., Li D. D., Wang C. S., Loh P. C., and Wang P. ‘The sliding mode load frequency  
379 control for hybrid power system based on disturbance observer’, *International Journal of Electrical  
380 Power and Energy Systems*, 74, 446-452 (2016).
- 381 [31] Lee Y., Kim S. H., and Chung C. C. ‘Integral sliding mode control with a disturbance observer for  
382 next-generation servo track writing’, *Mechatronics*, 40, 106-114 (2016).
- 383 [32] Rigatos G., Siano P., Zervos N., and Cecati C. ‘Control and disturbances compensation for doubly  
384 fed induction generators using the derivative-free nonlinear kalman filter’, *IEEE Transactions on  
385 Power Electronics*, 30(10), 5532-5547 (2015).
- 386 [33] Fei M. and Pal B. ‘Modal analysis of grid-connected doubly fed induction generators’, *IEEE Trans-  
387 actions on Energy Conversion*, 22, 728-736 (2007).
- 388 [34] Qiao W. ‘Dynamic modeling and control of doubly fed induction generators driven by wind tur-  
389 bines’, *Power Systems Conference & Exposition*, p. 1-8 (2009).
- 390 [35] Rezaeihaa A., Kalkmana I., and Blocken B. ‘Effect of pitch angle on power performance and aero-  
391 dynamics of a vertical axis wind turbine’, *Applied Energy*, 197, 132-150 (2017).
- 392 [36] Song D. R., Yang J., Cai Z. L., Dong M., Su M., and Wang Y. H. ‘Wind estimation with a non-  
393 standard extended Kalman filter and its application on maximum power extraction for variable  
394 speed wind turbines’, *Applied Energy*, 190, 670-685 (2017).
- 395 [37] Sanjoy R. ‘Performance prediction of active pitch-regulated wind turbine with short duration vari-  
396 ations in source wind’, *Applied Energy*, 114, 700-708 (2014).
- 397 [38] Juan R., Edgar L., Vicente V., David C., Ramon A., and Luis E. ‘Current-sensorless control of an  
398 SPWM H-Bridge-based PFC rectifier designed considering voltage sag condition’, *Electric Power  
399 Systems Research* 130, 181-191 (2016).
- 400 [39] Liu J., Wen J. Y., Yao W., and Long Y. ‘Solution to short-term frequency response of wind farms  
401 by using energy storage systems’, *IET Renewable Power Generation* 10(5), 669-678 (2016).

- 402 [40] Liao S. W., Yao W., Han X. N., Wen J. Y., and Cheng S. J. ‘Chronological operation simulation  
403 framework for regional power system under high penetration of renewable energy using meteorological data’, *Applied Energy* 203, 816-828 (2017).  
404
- 405 [41] Yao W., Jiang L., Wen J. Y., Wu Q. H., and Cheng S. J. ‘Wide-area damping controller for power  
406 system inter-area oscillations: a networked predictive control approach’, *IEEE Transactions on  
407 Control Systems Technology* 23(1), 27-36 (2015).